

Towards a comprehensive model for a resonant nanoelectromechanical system

S L Calvert^{1,2}, Y Shen^{2,3}, A B Sabater^{1,2}, S Mohammadi^{2,4}
and J F Rhoads^{1,2,5}

¹ School of Mechanical Engineering, Purdue University, West Lafayette, IN 47907, USA

² Birck Nanotechnology Center, Purdue University, West Lafayette, IN 47907, USA

³ Department of Physics, Purdue University, West Lafayette, IN 47907, USA

⁴ School of Electrical and Computer Engineering, Purdue University, West Lafayette, IN 47907, USA

⁵ Ray W. Herrick Laboratories, Purdue University, West Lafayette, IN 47907, USA

E-mail: jfrhoads@purdue.edu

Received 16 February 2015, revised 8 July 2015

Accepted for publication 9 July 2015

Published 17 August 2015



Abstract

The mass production and very large scale integration (VLSI) of micro/nanoelectromechanical systems (M/NEMS) requires the development and use of accurate models and simulations, which are capable of rapidly evaluating potential designs. Because of the large range of applications that have been proposed for M/NEMS, the most useful models are those that can accurately capture a system's response under widely varying input and operating conditions. This allows the M/NEMS devices to be treated as well understood circuit components in simulation contexts. It is towards this end that a first-principles based model is proposed for a resonant nanosystem inclusive of an electrostatically-actuated fixed-fixed beam resonator, test equipment and system parasitics. By encoding the algebraic and differential equations which describe the system into circuit components using Verilog-A, an experimental test setup was simulated using Spectre and subsequently compared to experimental results for qualitative validation of the model. The simulation was then used to investigate the behavior of a representative device for a basic input configuration that more closely represents a final-use scenario for the nanoresonator. Discrepancies between the commonly-employed experimental methodology and the practical final-use scenario are discussed and used as a platform to encourage the development of improved experimental methodologies, while also emphasizing the need for robust and accurate system-level models.

Keywords: resonator, modeling, nonlinear

(Some figures may appear in colour only in the online journal)

1. Introduction

The advantages that resonant micro/nanoelectromechanical systems (M/NEMS) provide in comparison to their purely-electrical counterparts, such as higher quality factors and narrower resonant bandwidths [1], has led to their proposed use in a variety of applications including tunable filters [2], logic elements [3], self-oscillators [4], transistors [5, 6], microscopic radios [7, 8] and mass sensors [9–12]. Working towards these ends, researchers have made a variety of advancements in M/NEMS by streamlining their fabrication

[13–17], modeling their performance, and to some extent enabling design [1, 4–9, 11, 13, 14, 16, 18–48].

As the basic understanding of different device designs and their attributes has matured, the need to begin looking at how to implement devices in their proposed end-use scenarios has grown. Research efforts began on a single-device scale for many systems [8, 34], but there is a pressing need to begin building the infrastructure for the design and fabrication of these devices at a mass production rate and in a very large scale integration (VLSI) context, in a fashion similar to existing electrical components. In order to achieve this, there

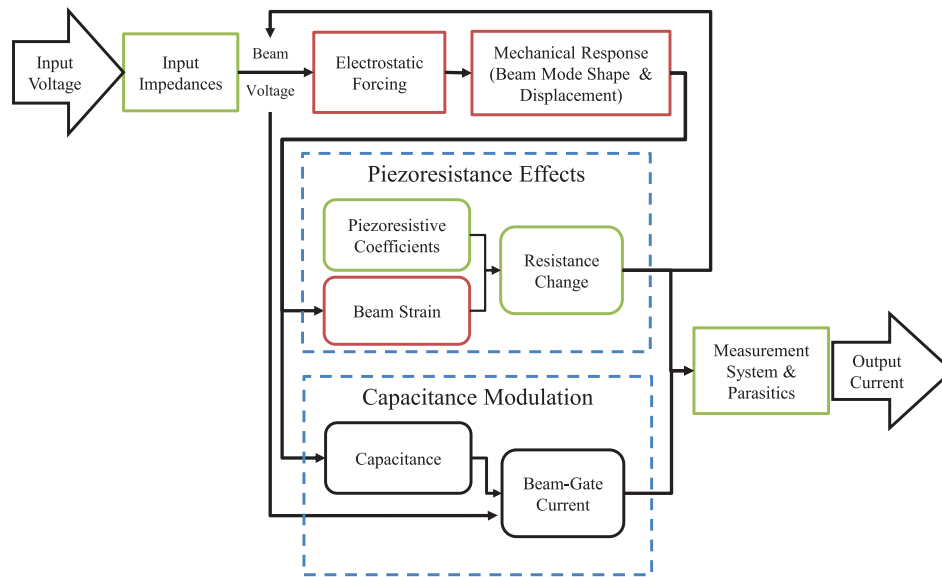


Figure 1. A high-level block diagram that illustrates the various interactions present in the actuation and measurement of the nanoresonator. The coupling between sub-domains motivates the need to analyze this device from a system-level perspective.

is a need for accurate, system-level electromechanical models of M/NEMS. This need points to experimentally-verified, first-principles based models as opposed to phenomenological descriptions, because of the desire to account for device behavior under a wide variety of input and operating conditions.

In the testing of electrostatic NEMS, it is common practice to measure the system's output at a frequency component resulting from the nonlinearities present in the electrostatic actuation, which mix various inputs [8, 9, 33, 36, 39, 41, 43, 45, 49]. There have been a variety of different mixing methods proposed for use, but they all share the advantage of addressing the difficulties that arise from attempting to identify mechanical resonances in the presence of various electrical output effects [35, 39]. The drawback for each method is the inherent reduction in the amount of information obtained from the system. If only the mechanical aspects of the system are under investigation, then a mixing approach may provide a suitable level of detail. However, models that have been verified to be accurate on the system level may reveal that the experimental mixing technique is insufficient for fully characterizing the system. In addition, stopping at developing a model that represents the velocity or displacement of M/NEMS will likely fail to provide insight into even the qualitative nature of the electrical response, as shown in [40] where the mechanical and electrical responses of the same system are qualitatively different. Likewise, a model that only describes the currents driven by the dominant electromechanical transduction mechanism may fall short of describing the true response by ignoring the feedback and damping of the full circuitry and mechanics involved. Therefore, any experimentation and modeling efforts should ideally account for the full electrical system of the test setup to allow for the later extraction of an isolated device model that could be correctly implemented with any other circuit.

In order to achieve mass production, and VLSI use, of M/NEMS, the model of any given device must be able to integrate with other electrical components to predict a system-level response. The use of the various model components and system-level effects in a standard commercial circuit simulator allows for fast verification and tuning of the model behavior, particularly when comparing to experimental results. It also serves as a direct pathway to the future use of the device model on a larger scale. The ease with which a properly implemented device simulation can be integrated with other components also opens the door for the evaluation of the next steps towards practical implementations of a device, such as impedance matching or filter design.

The present work seeks to develop a first-principles based, system-level model and circuit simulation for the fixed-fixed beam nanoresonator system that was first presented in [14]. This system produces a measurable output through coupled capacitance modulation and piezoresistive effects. Nonlinear responses can be obtained even at low forcing voltages [47], which allows for intriguing behaviors such as the electrostatic tuning of the resonant frequency [48] with slight changes in the input. Features such as this pose an interesting design challenge while also being a powerful tool for circuit developers. The interactions between the different domains present in the system of interest are visualized in figure 1. The need to interpret the device on a system level is underscored by the fact that the deflection of the beam inherently results in changes to the beam currents, as well as its voltage. These changes then alter the forcing of the beam, which changes its deflection, and further changes the electrical state of the device. These interactions are shown in figure 1 as feedback between the various transduction methods and the beam voltage. Note that unless the device is viewed from a systems' perspective, these rich dynamic interactions will not be properly captured. After presenting models for the beam motion, the electrostatic forcing

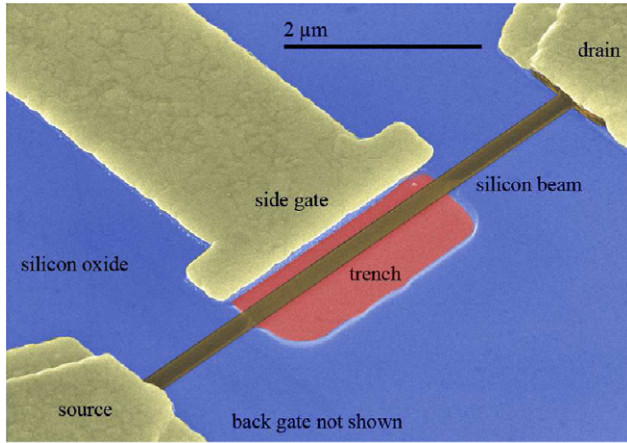


Figure 2. A false-color scanning electron microscope image of a representative device. Image adapted from [14].

and the current generation effects, this work looks at the results of implementing these fundamental aspects of the nanoresonator together, using Verilog-A and Spectre. This approach is used to recover estimates of the system response and generate qualitative comparisons to various experimental data.

2. Device-level model

The model presented herein was developed for a NEMS resonator (figure 2) of the design presented in [14]. Experiments were carried out to characterize the behavior of the device and were qualitatively compared to simulations of the developed model. Specific details on the fabrication and design of the device can be obtained in the aforementioned reference. The device was designed with a fixed-fixed silicon beam etched above an electrode (the back gate) with another electrode on the side of the beam (the side gate). While the device can be forced by both gates simultaneously, in order to better isolate the dynamics at play, only out-of-plane excitation by the back gate has been considered here.

2.1. Mechanical modelling

Prior works, such as [35, 45, 53], have demonstrated that Bernoulli–Euler beam models capture the mechanics of nanobeams within a reasonable level of accuracy. While recent works have indicated that non-local strain models may improve the accuracy of such mechanical models [50–52], at the present juncture there is not enough experimental evidence in the literature to justify the added fidelity. Accordingly, the classical Bernoulli–Euler model is expanded here to capture nonlinear mid-plane stretching and residual stress—assumed to be constant throughout the beam—which are substantial when later transduction effects are considered. The system has two gates, and thus could be forced in two directions, but the stipulation that only the back gate would be used for forcing allows for the simplification of the system model presented here.

Using the coordinate system laid out in figure 3, and assuming a slender beam (that is, assuming $\sqrt{I/A}$ is small,

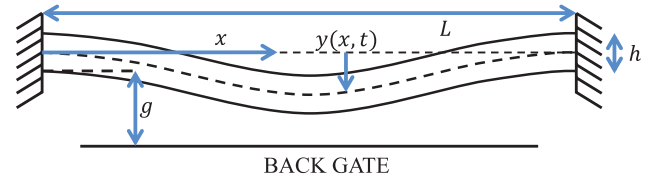


Figure 3. Beam variables for a back gate only excitation scenario. The electrostatic force acts between the bottom of the beam and the back gate.

where I is the moment of inertia and A is the area of the beam cross section), the equation of motion,

$$\rho wh \frac{\partial^2 y(x, t)}{\partial t^2} + c \frac{\partial y(x, t)}{\partial t} + EI \frac{\partial^4 y(x, t)}{\partial x^4} - T \frac{\partial^2 y(x, t)}{\partial x^2} = F(x, t) \quad (1)$$

is obtained, where L , w and h are the length, width, and height of the nanobeam, respectively, while ρ is the mass density and E is the modulus of elasticity for the material. I is the moment of inertia for the beam, which for a rectangular cross section in out-of-plane motion is

$$I = \frac{1}{12} wh^3. \quad (2)$$

$y(x, t)$ is the deflection of the beam at time t at a distance along the beam, x . c is the specific viscous damping coefficient for the beam. T represents the axial forces within the beam and is defined as

$$T = S_r wh + \frac{Ewh}{2L} \int_0^L \left[\frac{\partial y(x, t)}{\partial x} \right]^2 dx. \quad (3)$$

This term produces third-order nonlinearities in the equation of motion. Here, S_r is the average, uniform, residual stress in the beam and the integral term captures effects due to mid-plane stretching.

Because the excitation combinations considered here are only near the first eigenmode of the beam, the single-mode approximation,

$$y(x, t) = \phi(x)z(t), \quad (4)$$

is used to simplify the partial differential equation presented here into an ordinary differential equation using Galerkin methods. The mode shape, $\phi(x)$, is normalized such that the deflection of the beam midpoint is unity, and can be written as,

$$\phi(x) = a \sin\left(p \frac{x}{L}\right) - \cos\left(p \frac{x}{L}\right) - a \sinh\left(p \frac{x}{L}\right) + \cosh\left(p \frac{x}{L}\right), \quad (5)$$

where a and p are constants determined by the mode number and boundary conditions. The normalization scheme allows $z(t)$ to represent the displacement of the midpoint. This is useful for developing the electrostatic forcing and current modulation models in sections 2.2 and 2.3.1, respectively.

Developing a reduced-order model through the aforementioned Galerkin approach results in

$$\begin{aligned} & \rho wh \int_0^L \phi^2(x) dx \ddot{z}(t) + c \int_0^L \phi^2(x) dx \dot{z}(t) \\ & + \left[EI \int_0^L \phi'''(x)\phi(x) dx - S_r wh \int_0^L \phi''(x)\phi(x) dx \right] z(t) \\ & - \frac{Ewh}{2L} \int_0^L [\phi'(x)]^2 dx \int_0^L \phi''(x)\phi(x) dx z^3(t) \\ & = \int_0^L F(x, t)\phi(x) dx, \end{aligned} \quad (6)$$

where

$$(\bullet)' = \frac{\partial(\bullet)}{\partial x}, \quad (\dot{\bullet}) = \frac{\partial(\bullet)}{\partial t}. \quad (7)$$

Note that the residual stress in the beam from fabrication, S_r , alters the effective beam stiffness. Also note that the cubic nonlinearity due to mid-plane stretching creates a nonlinear, mechanical hardening effect.

Equation (6) requires an understanding of the specific damping coefficient, c , of the beam. There are several contributions to damping for a NEMS resonator spanning both intrinsic and extrinsic phenomenon, including squeeze film damping, anchor loss, thermoelastic dissipation and phonon-phonon interactions. Various estimates have been developed for a variety of these factors [24, 25, 37, 38, 54, 55]. Reference [54] suggests that any form of viscous damping is negligible for testing at low pressures (such as $<75 \mu\text{Torr}$, which was used for the experimental data presented here). Further estimation of the damping is also reliant upon the quality of the fabrication and the materials of the devices considered. For the simulation, order of magnitude estimates of c were used to develop an approximation which presented an appropriate amplitude response given estimates for all other system parameters.

2.2. Electrostatic forcing

The nanobeam experiences a distributed electrostatic force arising from the potential difference between the gate and the beam. Works such as [18] have shown that a standard parallel-plate model fails to completely represent the actual forcing that the beam experiences (as validated by a two-dimensional finite element solution) and proposes several expanded models to account for the beam's mode shape. Likewise, [56] presents an improved capacitance model which uses fringe field corrections to account for the electric field behavior around the finite cross-section of a nanobeam. Each of these capacitance models are directly related to the electrostatic forcing experienced through

$$F_{\text{total}}(t) = \frac{1}{2} \frac{\partial C}{\partial y(x, t)} V^2(t), \quad (8)$$

where C is capacitance [39], and can be shown to greatly improve the model accuracy as compared to the basic parallel-plate approximation.

The model in [56] is primarily shown to improve the accuracy of pull-in voltage predictions. In contrast, the model

presented in [18] is shown to be accurate for small deflections of a two-dimensional beam. Because the majority of commercial end-use scenarios for these systems will likely operate far from the pull-in voltage, the best model from [18] was selected as the sub-component model to be used herein. The selected model is a 4th-order perturbation of the spatial function describing the potential between the gate and the beam. For present purposes, the forcing definition developed in [18] was dimensionalized and expanded in a Taylor series around $z(t) = 0$, retaining terms up to the 3rd-order to match the accuracy of the mechanical model. The expansion is necessary to allow the forcing term to be properly integrated when the Galerkin approach is applied to the equation of motion. It is important to note that this implies that the model will no longer properly predict the pull-in behavior of the system and should only be used with small deflections. This is viewed by the authors as an acceptable trade-off given that most commercial resonators will likely be driven far from pull-in, unless utilized in switching or logic applications, which are not of direct interest here.

The final dimensionalized representation of the forcing, as obtained from [18], is

$$\begin{aligned} F(x, t) \approx & \frac{\epsilon_0 w V^2(t)}{90g^5} (45g^3 + \{90\phi(x) \\ & - 2g^2[15\phi''(x) + g^2\phi'''(x)]\}g^2z(t) \\ & + \{135g\phi^2(x) + g^3[-15\phi'^2(x) + 3g^2\phi''^2(x) \\ & + 4g^2\phi'''(x)\phi'(x)] \\ & + 2g^3[-15\phi''(x)\phi(x) + g^2\phi'''(x)\phi(x)]\}z^2(t) \\ & + [180g\phi^3(x) - 30g^2\phi'^2(x)\phi(x) - 30g^2\phi''(x)\phi^2(x) \\ & + 48g^4\phi''(x)\phi'^2(x)]z^3(t). \end{aligned} \quad (9)$$

It should be noted that the forcing is proportional to $V^2(t)$ and this dependence enables the device to be used as a mixer, as discussed in section 1. Here $V(t)$ is the voltage between the beam and the back gate. It is assumed that the midpoint voltage of the beam adequately approximates an equivalent average voltage that sufficiently describes the forcing of the beam. The application of an amplitude-modulated ac signal, with frequencies $\omega_c, \omega_c \pm \omega_m$, and a dc bias results in beam frequencies of $i\omega_c \pm j\omega_m$, for $i, j \leq 2$ and a static deflection. The dependence of the forcing on both the potential difference between the beam and gate, as well as the beam's deflection, is what contributes to the electrostatic tuning of the resonant frequency. Combining the mechanical and electrostatic forcing terms, the full nonlinear equation of motion for the resonator,

$$\begin{aligned} B_0 \ddot{z}(t) + B_1 \dot{z}(t) + [B_2 - f_c(t)f_1]z(t) - f_c(t)f_0 - f_c(t)f_2 z^2(t) \\ - [B_3 + f_c(t)f_3]z^3(t) = 0 \end{aligned} \quad (10)$$

is produced. The full description of the coefficients for equation (10) are provided in appendix A. Equation (10) shows how the electrostatic forcing of the nanoresonator produces a large portion of the system's rich dynamics within the mechanical sub-domain.

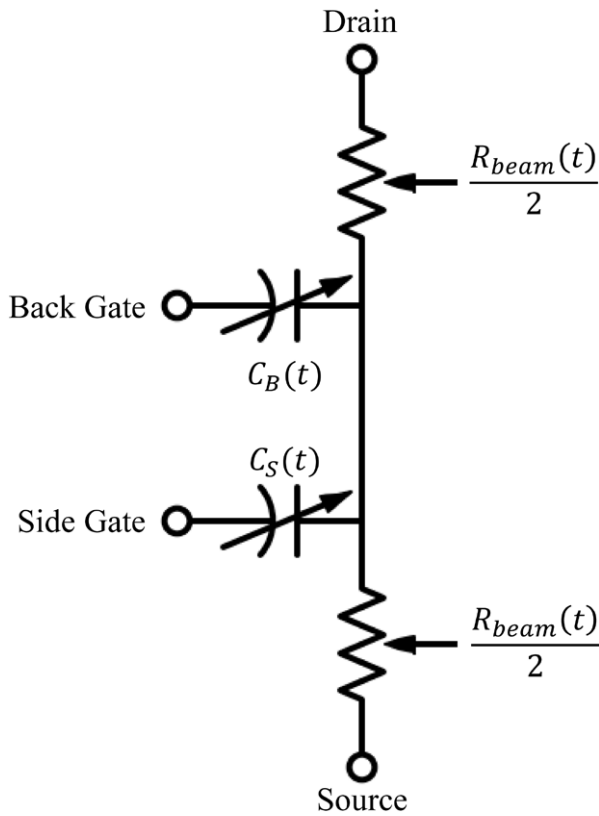


Figure 4. An equivalent electrical schematic for the nanoresonator. The capacitive effects, $C_B(t)$ and $C_S(t)$, are assumed to act based upon the voltage at the midpoint of the beam. The varying beam resistance, $R_{beam}(t)$, is correspondingly split as a representation of the two beam halves. Both effects are coupled through their dependence upon the beam deflection. The source and drain ports correspond to the contacts at the ends of the beam, while the gate ports are the contacts at the associated gate electrodes.

2.3. Device-level electrical behavior

The vibration of the beam results in the modulation of the capacitance between the beam and the gate. Likewise, the periodic strain within the beam as it vibrates can result in resistance changes through geometric and piezoresistive effects. Collectively, these effects lead to a device that can produce resonant currents when the potential between the beam and gate varies at frequencies corresponding to the resonant frequency of the beam. The circuit model presented in figure 4 illustrates the ways the various parts of the device interact, representing the capacitance modulation and piezoresistive effects as variable capacitors and resistors whose values are dependent upon the beam’s displacement. The two effects are directly connected, as the electrostatic forcing, and thus capacitance, determines the beam deflection and strain, which in turn determines the effective resistance of the beam. This then alters the potential difference controlling the forcing of the beam, effectively creating an electromechanical feedback loop. Accordingly, it is important to consider the actual voltage across the beam, rather than the direct ac and dc inputs to the system. While it is possible to design a device that uses only one of these transduction mechanisms, whether

by mechanically actuating the beam to produce only piezoresistive effects [41] or by focusing on the currents flowing through a gate to isolate capacitive effects [13, 36], the experimental set-up presented here measures the current flow along the length of the beam, resulting in the need to study a combination of both effects [6].

2.3.1. Capacitance modulation. The capacitance of a system is directly related to the electrostatic forcing experienced, as discussed in section 2.2. Therefore, based upon the forcing model already selected, the beam capacitance was also developed in [18]. Krylov and Seretensky present the capacitance in a nondimensionalized form of $\partial C/\partial x$, which is dependent upon $1/g - y(x, t)$ after dimensionalization. Here, g is the static gap distance between the gate and the beam. In order to integrate along the length of the beam to obtain C_B , the capacitance between the beam and the back gate, the terms in $\partial C/\partial x$ were expanded in a Taylor series expansion around $z(t) = 0$, keeping terms up to $z^3(t)$ in line with the mechanical and forcing expansions (sections 2.1 and 2.2, respectively) to produce

$$C_B(t) \approx \frac{\epsilon_0 L}{g} [L + \kappa_1 z(t) + \kappa_2 z^2(t) + \kappa_3 z^3(t)] \quad (11)$$

where ϵ_0 is the permittivity of vacuum and the constants κ_1 through κ_3 can be found in table A2. As with the electrostatic forcing, this approximation of the capacitance has an improved response to the beam’s curvature, as compared to a classical parallel-plate model, but does not include corrections for fringing fields.

Combining the general definition of the charge present in a capacitor,

$$Q_{cap}(t) = V(t)C(t), \quad (12)$$

with the general definition of current,

$$i(t) = \frac{dQ}{dt}, \quad (13)$$

produces the current flowing through the capacitor formed between the gate and the beam,

$$i_B(t) = \dot{C}_B(t)V(t) + C_B(t)\dot{V}(t). \quad (14)$$

Here, $Q_{cap}(t)$ is the charge present in the capacitor. A similar process can be used, with the proper geometry, to determine the capacitance of the side gate, $C_S(t)$, for those cases where it is desirable to include it. The variable capacitance enables the capacitor to exhibit a resonant behavior for voltages at the same frequencies as the beam’s resonant frequency. Since $z(t)$ contains frequency components proportional to those present in $V^2(t)$ and $C_B(t)$ and $\dot{C}_B(t)$ contain frequency components related to up to $z^3(t)$, the capacitance and its time derivative will fluctuate with frequencies related to those present in $V^6(t)$. Consequently, the current flowing between the beam and gate inherently has frequency components associated with those present in $V^7(t)$. This causes a final signal with many more harmonics than the original input, $V(t)$, resulting in very small currents at any single frequency as the input power is spread throughout the harmonics. Depending on the excitation and

measurement scheme used with the device, this current could be considered a parasitic as it flows between the beam and gate instead of directly through the beam.

2.3.2. Piezoresistivity. The current through the beam also varies as the resistance of the beam is modulated by mechanical deformations, due to geometric and piezoresistive effects. The piezoresistive properties of silicon were thoroughly described by Kanda in [57]. The piezoresistive effect in doped silicon is dependent on the strains parallel and perpendicular to the current flow. It is important to note that the piezoresistive variations experienced by the device are primarily a nonlinear phenomenon. The strains in the beam due to linear deflections are equal and opposite on either side of the neutral axis, causing a net zero strain in any instantaneous cross section and no net resistivity change [41]. In contrast, mid-plane stretching causes a lengthening of the neutral axis and thereby induces an average strain along the entire beam, resulting in a uniform change in the resistivity. Therefore, it is the strain due to mid-plane stretching that must be determined for use in finding the instantaneous resistance values. While this strain is typically small, the piezoresistive coefficients can be large enough to cause piezoresistivity to be a dominant transduction mechanism. As described in [41], the strain from mid-plane stretching, $\epsilon(t)$, can be shown to be

$$\epsilon(t) = \frac{1}{2L} \int_0^L \left[\frac{\partial y(x,t)}{\partial x} \right]^2 dx. \quad (15)$$

For a fixed-fixed beam and assuming a first-mode resonance, [41] shows equation (15) to simplify to

$$\epsilon(t) = 2.44 \left[\frac{z(t)}{L} \right]^2 \quad (16)$$

for the single-mode approximation. This approximation was verified by numerical comparison to the strain model presented in [58], which derives a strain equation by analyzing the transverse and axial strains arising during deflection. The different approaches were found to be in excellent agreement with a net relative error, when tracking the strain in the beam over 1 ms of vibration, of 0.047%. The dependence of the strain on the square of the displacement captures the fact that the beam undergoes two periods of strain for every period of beam deflection. However, when it is considered that the steady-state vibration already has frequency components relating to both the original modulation terms, as well as the inter-modulation and down-mixed terms arising from electrostatic forcing, then it becomes clear that the frequency terms present in the resistance fluctuations will be even more numerous.

Because of the crystal structure of silicon, the direction of the crystal lattice with respect to the current flow has a large impact on the piezoresistive effect observed. For this application, the transverse and shear stresses can be assumed to be negligible in comparison to the axial stresses and thus the beam resistance equation becomes

$$R_{\text{beam}}(t) = R_0[1 + \epsilon(t)G_R], \quad (17)$$

where R_0 is the nominal beam resistance given by

$$R_0 = \frac{\rho_t L}{wh}. \quad (18)$$

Here, ρ_t is the nominal resistivity of the doped silicon. G_R in equation (17) is the resistance gauge factor,

$$G_R = 1 + 2\nu + E\pi_L. \quad (19)$$

This gauge factor captures both geometric effects, represented by $(1 + 2\nu)$, where ν is Poisson's ratio for the beam material, and piezoresistive effects, encompassed by $E\pi_L$. Here, π_L is the effective longitudinal piezoresistive coefficient, which introduces the dependence of the piezoresistive effect on crystal orientation and other parameters, such as doping and temperature [57]. Further derivation of the proper π_L values for a unique orientation, doping level and temperature can be found in [57]. In [46], He and Yang show the effective piezoresistive coefficients in silicon nanowires to be highly dependent upon the diameter of the nanowires. They show that the piezoresistive effect is greatly amplified, compared to the effect in bulk silicon, by having smaller diameter nanowires. Gauge factors as large as 2000 are presented, while the values for bulk silicon are traditionally in the hundreds. Because this effect has yet to be fully investigated for silicon nanobeams, it is difficult to interpret at what size the values for bulk silicon become inaccurate. As such, the size effects were ignored and only the values associated with bulk silicon were utilized here in order to present a more conservative model of the potential effects from piezoresistance.

The final representation of the beam resistance,

$$R_{\text{beam}}(t) = \frac{\rho_t L}{wh} \left\{ 1 + 2.44 \left[\frac{z(t)}{L} \right]^2 (1 + 2\nu + E\pi_L) \right\}, \quad (20)$$

clearly shows the dependence of the beam resistance on $z^2(t)$. As described in section 2.3.1, the dependence of $z(t)$ on $V^2(t)$ implies that the fluctuations in resistance will have frequency components associated with those present in $V^4(t)$. Unlike this effect in the capacitance modulation, the increased number of frequencies in the resistance fluctuations should have a net effect of increasing the current flow at any given frequency by reducing the resistance at that frequency through the same power spreading effects present in the capacitance modulation context (section 2.3.1).

3. System-level modeling

Though the model developed above may provide the most relevant dynamics for current modulation, it is only a subset of the full test system. The full experimental setup is represented in figure 5 and was fully described in [14]. For actuation, an amplitude-modulated ac signal is applied to the beam through the drain pad while a dc bias is applied to the back gate (see figure 2). The resulting current through the beam was measured by a lock-in amplifier at the modulation frequency, f_m , which is produced by the nonlinearities in the electrostatic forcing and other electromechanical interactions. A typical experimental test consisted of slowly increasing or decreasing

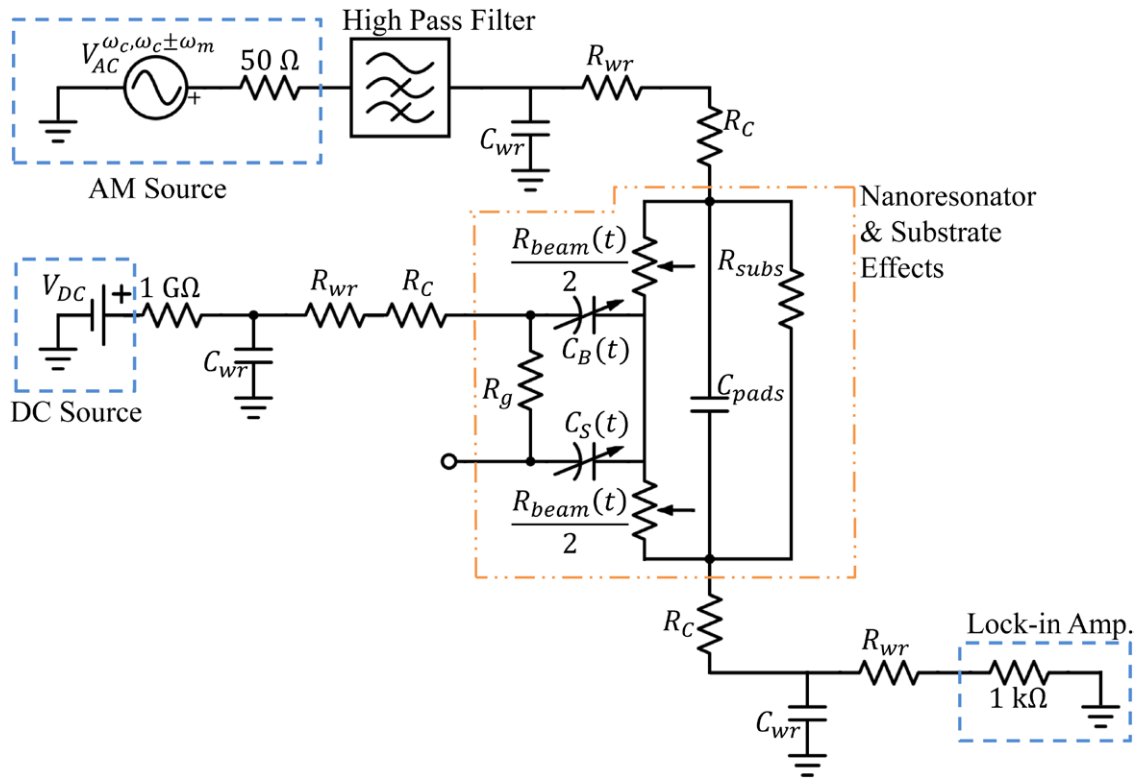


Figure 5. The final circuit schematic of the excitation system, device representation, parasitics and measurement system. The side gate is left floating in order to simplify experimentation.

the carrier frequency of the modulated signal and recording the resulting amplitude and phase profile for the modulation frequency. The required signal sources, measurement systems and other parasitics must be considered in the model to later achieve an appropriate understanding of the isolated device dynamics. The schematic in figure 5 was developed to account for these interactions. Note that the inclusion of the aforementioned subsystems implies that the voltages forcing the beam are not the direct inputs applied to the system. Rather, the steady-state input to the beam will be attenuated and have additional frequency components arising from the beam nonlinearities.

Due to the device substrate failing to provide proper insulation between the source and drain pads, a resistance R_{subs} , was included herein to model the possibility of currents bypassing the beam to contribute a direct feed-through current to the final output. Regrettably, a resistance measurement of a device between the source and drain reveals the combined resistance of the beam and substrate, so a unique identification of the substrate resistance was not directly obtainable. Several devices experienced some amount of finite resistance, and thus electrical coupling, between the side and back gates, represented in figure 5 as R_g . While this does result in a potential difference between the beam and the side gate, the geometry of the system and the leakage resistance are such that it is reasonable to expect no mechanical actuation of the beam in-plane comparison to that experienced in the out-of-plane vibration. The side gate’s electrical presence is potentially relevant as a parasitic current pathway within the circuit, and is included in the simulation to this extent. It is interesting to note that

grounding the side gate would create a pathway to ground for the back-gate bias, reducing—and potentially eliminating—the bias’ effect on the forcing of the beam.

The measurement system also exhibited several parasitics affecting the final measurable output. The contact of the probes with the pads on the device resulted in a contact resistance, R_C , for every connection made. While the back gate was excited through the bottom of the substrate, the contact with the probe station chuck was imperfect and featured a similar resistance. Unfortunately, since the exact resistances of the device components are unknown, the contact resistances can only be experimentally estimated with low fidelity. Because of the small size of the contact resistances in relation to the device resistance, it was assumed that a single average resistance value could be used for all of the various contacts.

The probes and pads at the source and drain were also close enough to introduce a capacitive bypass of the beam, C_{pads} . Similar to the substrate resistance, but frequency dependent, this created a parallel path for current to bypass the beam. The value of this capacitance was estimated by assuming the probe tips were parallel plates placed at the ends of the source and drain pads. It was also estimated by raising the probes directly above the contact pads and looking at the response between the probes.

The rest of the circuit consists of approximations for the various sources and measurement devices. The ac sources in the model represent the output of a modulation-capable signal source through a high-pass filter. The high-pass filter was included experimentally in an attempt to prevent any leakage from the modulation signal source at the modulation

frequency. Initial experimentation and simulations showed signs that the leakage voltage was not being fully attenuated since a non-zero off-resonant current was consistently measured, and the response was affected by the presence of the high pass filter. Therefore, instead of capturing the full characteristics of the high pass filter, the system was modeled as having an ideal, amplitude-modulated signal with a constant amplitude leakage voltage, V_{leak} , at the modulation frequency. The lock-in amplifier, an SRS-830, was modeled as a 1 k Ω resistor to ground, as suggested in the device documentation. While the probe station has triaxial cable outputs, the lab equipment was uniformly equipped with biaxial junctions. Bufferless adapters were used and the parasitic prevention of the triaxial cables was lost. Therefore, the wires of the system were all considered as a capacitance to ground, C_{wr} , followed by a resistance, R_{wr} . The specific capacitance of the cables was both obtained from the supplier and measured in the lab as verification. The resistance of the wires was also measured and an average resistance was used for each implementation in the model. The 1 G Ω resistor following the gate source was used to prevent an excessive current flow through the device in the case of beam pull-in.

4. Results

In order to compare the results produced by the modeled system and those found experimentally, it was prudent to compile and implement the various aspects of the presented model by programming the corresponding differential and algebraic equations using Verilog-A to form two separate blocks of code. One captured the electrostatic effects and beam motion, by accepting the beam-gate voltage as an input and determining the beam displacement, capacitance and current flow as outputs. The other component accepted the voltage drop across the beam and the beam displacement as inputs to determine the current through the beam when accounting for piezoresistive effects. These components represented the variable capacitors and resistors in figure 4, respectively. The Verilog-A components were combined with the rest of the circuit (figure 5), and simulated using the Spectre (a derivative of the SPICE simulator) harmonic balance solver to determine the steady-state outputs of the system. The harmonic balance solver used a two-step approach to generate this output, first finding an initial operating point and then using Newton methods to converge upon steady-state values. For the typical simulations presented here, the harmonic balance approach required consideration of at least 8 harmonics for both the carrier and modulation frequencies to produce a solution which did not change upon the addition of further harmonics. Depending on the amplitude of the response, either transient-aided solving or source stepping homotopy methods were implemented to achieve an initial operating point that would generate a converged steady-state output. Generally, the transient-aided approach was more reliable, but significantly slower (~ 15 min/2 MHz sweep around resonance), than source-stepping (~ 5 min/2 MHz sweep around resonance). These solving times can be traced to the large number of harmonics needed to accurately capture the nonlinear behavior and complexity

associated with the interaction between the piezoresistive and capacitive sections of the beam. Furthermore, the small signal size, often on the picoAmpere scale, required tight tolerances and lead to the need for more iterations in the harmonic balance solution and thus a slower result. In plotting the output, it was possible to generate plots directly reporting the same information acquired experimentally. These plots depict changes in the amplitude and phase of the signal at the modulation frequency as the carrier frequency was varied. The simulation was also capable of producing transient waveforms and other results, which are potentially beneficial, but the harmonic balance results provided the most direct comparisons to experimental data.

The parameters for the model were selected to be similar to the resonator tested by Yu in [14]. That is, the beam had a height, h , of 110 nm, and was in the $\langle 111 \rangle$ orientation, resulting in $E = 187.5$ GPa and $\nu = 0.17$ [59], where ν is Poisson's ratio. The back and side gates have nominal gap sizes of $g_b = 144$ nm and $g_s = 200$ nm, respectively. The beam was considered to have no residual stresses present. $\rho = 2330$ kg m $^{-3}$ is the density of silicon. The beam was approximated to have a value of $c \approx 0.6E - 6$ kg (m.s) $^{-1}$. Different tests were compared with different beams, using dimensions of either $L = 6.3$ μm , $w = 120$ nm or $L = 4$ μm , $w = 180$ nm. The amplitude modulation of the input signal was kept at a consistent modulation index, the parameter defining the height of the side bands in the modulated signal, $m = 0.5$, and modulation frequency, $f_m = 1$ kHz. V_{ac} , V_{dc} and f_c , the amplitude of the carrier signal, the dc bias, and the carrier frequency, respectively, were used as the inputs to the system. Several basic electrical parameters, such as R_{wr} , R_c , R_g , and C_{wr} were measured from the experimental setup or obtained by other approximations, as discussed in section 3. It should be noted that many of these values, and those not listed here but included in table A3, have some measure of uncertainty. For example, there are fabrication tolerances associated with the physical dimensions of the device. Other parameters, such as the residual stress in the beam, are highly uncertain (see section 3).

While the device design described herein has the potential for both in- and out-of-plane motion, allowing for the exploitation of whirling effects and multiple resonances, each associated with a plane of excitation [27], only back-gate excitation was considered here. This allowed the model to be developed while focusing on only a single resonance, and vastly reduced the amount of experimentation needed. Understanding a single-gate excitation case forms the basis for understanding and developing a coupled-mode model. Unfortunately, some of the tested devices did not have the proper isolation between the side and back gate, and thus had some finite level of resistance between them (R_g was experimentally measured as 263 k Ω for the simulated device). This allowed a voltage applied to the back gate to also generate a voltage on the side gate, and vice versa. This potentially introduced in-plane vibrations in addition to the desired out-of-plane motion. The differences between the side and back gap distances and surface areas resulted in 0.475 times as much force from the side-gate as from the back-gate for the

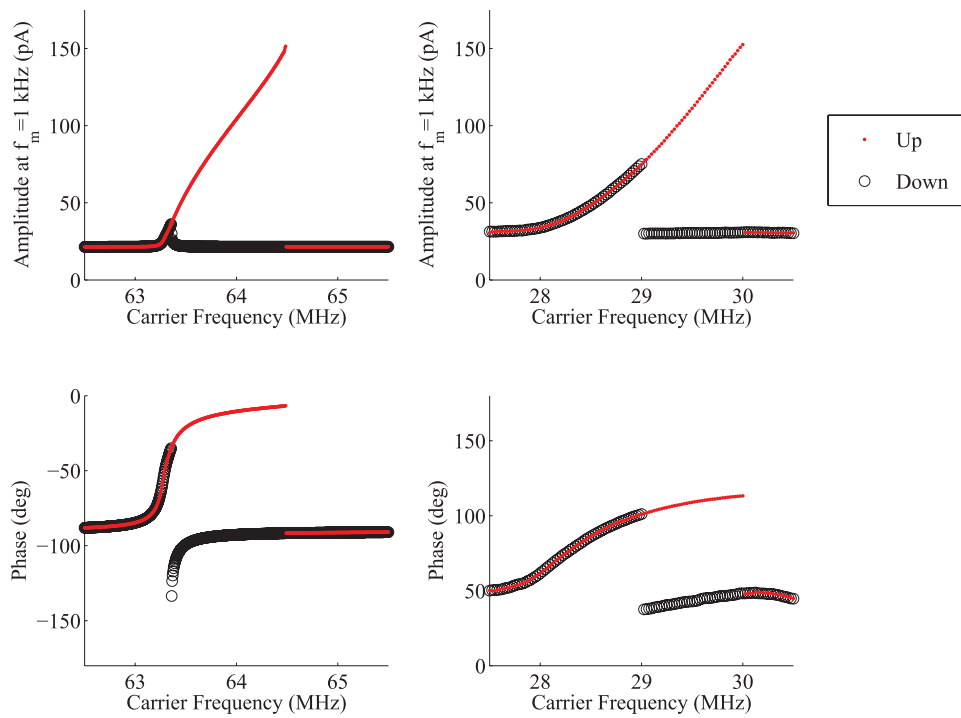


Figure 6. A comparison of the simulated (left) and experimental (right) results for both response amplitude (top) and phase (bottom). The results are collected at the modulation frequency of the input, here 1 kHz, as the carrier frequency is either increased or decreased around resonance. Note that no high pass filter or current limiting gate resistor were used when obtaining the present experimental data. Here, $V_{dc} = 6$ V, $V_{ac} = 40$ mV_{rms}, $L = 4$ μ m (Note, per the discussion in the text, this value may be underestimated.), and $w = 180$ nm.

same voltage, based upon a parallel-plate estimation. This arose from a 0.917 times smaller surface area, and a 1.389 times larger gap. When the magnitude of the voltage drop across the resistor formed by the leakage between the gates was also considered, it was assumed that a voltage applied to the back gate of the device would not produce enough force through the side gate to cause significant actuation of the in-plane resonance and only out-of-plane motion was considered. However, the static capacitance for the side gate was still included in the model since it remains reasonable to simulate the side gate's electrical effects.

Simulated magnitude and phase responses were qualitatively compared to experimental results reported herein, as well as those previously presented in [14]. Figure 6 shows the similarity between the simulation and the experimental response of a 4 μ m beam, without any parameter estimation for highly uncertain parameters. While quantitative shifts exist, it is probable that these differences could be attributed to the variability of the nominal system parameters. The most notable discrepancy is that the resonant frequency predicted by the simulation is much larger than what is seen experimentally. However, when a scanning electron micrograph was taken of the beam location after testing was completed, figure 7, it was found that the trench, including the visible undercutting at the edges, measured approximately 4 μ m corresponding to the theoretical length of the beam and thus the length used for the simulation in figure 6. Yet, it was noted that the pad-to-pad distance was roughly between 5.7 and 6 μ m. If the simulation is instead run for a beam of length $L = 5.9$ μ m, the frequency and bandwidth more closely matches what is observed experimentally, as seen in figure 8. This would

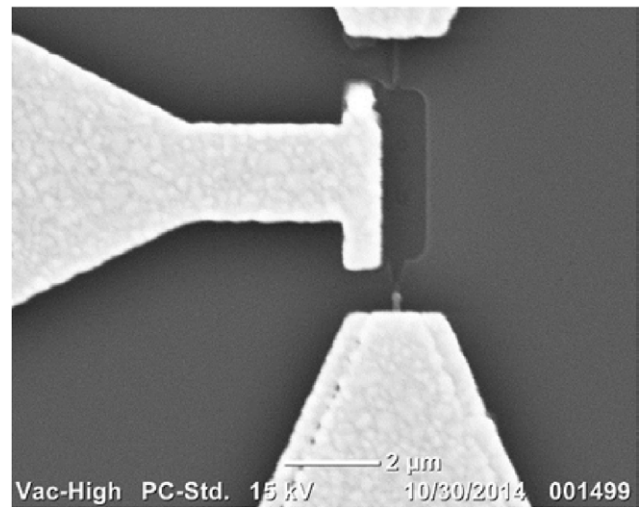


Figure 7. An SEM of the beam location for the experimentally-tested device. The beam was destroyed following testing, but the trench size gives an estimate of the suspended length of the beam. The trench length, including visible undercutting, is approximately 4 μ m. The pad-to-pad length of the beam would be roughly 5.7 to 6 μ m. Photo Credit: Hossein Pajouhi.

suggest that the entire length of the beam was released from the substrate during the fabrication process, rather than just across the trench.

The discrepancies in figure 6 can alternatively be diminished by making variations to the residual stress and specific damping coefficient, which are both very difficult to measure and predict. Variations in these parameters can shift the simulated response to a similar frequency and amplitude, as seen

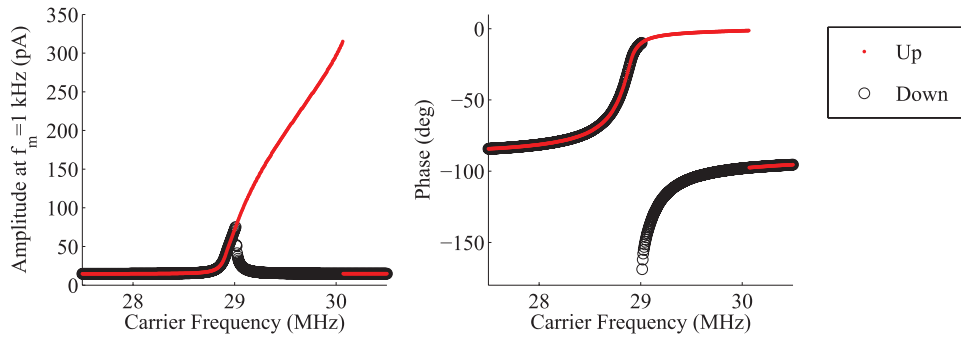


Figure 8. The simulated response amplitude (left) and phase (right) collected at the modulation frequency of the input, here 1 kHz, as the carrier frequency is either increased or decreased around resonance. Note, $V_{dc} = 6\text{ V}$, $V_{ac} = 40\text{ mV}_{rms}$, $L = 5.9\text{ }\mu\text{m}$, and $w = 180\text{ nm}$.

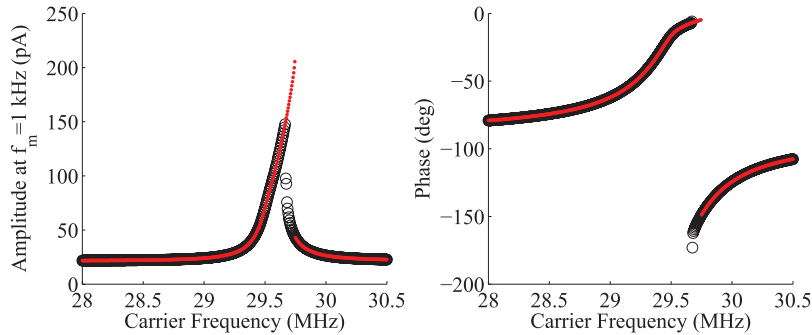


Figure 9. The simulated response amplitude (left) and phase (right) collected at the modulation frequency of the input, here 1 kHz, as the carrier frequency is either increased or decreased around resonance. Note, $V_{dc} = 6\text{ V}$, $V_{ac} = 40\text{ mV}_{rms}$, $L = 4\text{ }\mu\text{m}$, $w = 180\text{ nm}$, $S_r = -375\text{ MPa}$ and $c = 6\text{ }\mu\text{kg m}^{-1}\text{ s}^{-1}$.

in figure 9. In this case, the differences in bandwidth and off-resonant current could be explained through variations in a combination of other parameters, most directly involving the length, height and nominal gap of the beam. Other parameters, such as the leakage voltage at the modulation frequency, play a large role in determining the nonzero off-resonant response as well as the shape of the phase response. Similarly, the amplitude of the response could be shown to be highly dependent upon the effective piezoresistive coefficient, which was shown in [46] to be dependent on diameter for a silicon nanowire, but has not been fully characterized for nanobeams. It was anticipated that, given the proper parameter set, the model would accurately provide the down-mixed response near the first-mode beam resonance.

The capability for the model to approach the proper results with a correct parameter set can be justified by an analysis of the system’s sensitivities to the most uncertain parameters. For this system, those parameters primarily relate to the beam itself, since there is a large degree of uncertainty with regard to the initial state of the wafer and the fabrication processes. Figure 10 demonstrates the effects of a 5% variation from the nominal value for a variety of parameters. Even these slight deviations from the nominally simulated values can lead to significant quantitative shifts in the observed response, while maintaining a qualitatively-similar response shape. Increasing the length of the beam or the compressive residual stress decreases the peak frequency, while increasing the peak amplitude. The opposite is true for an increase in the height of the beam. An increase in the modulus of elasticity (which could arise from a beam etched in an incorrect orientation

with respect to the silicon crystal) increases the peak frequency while marginally changing the response amplitude. A decrease in the elasticity decreases the peak frequency and increases the amplitude of the response. Decreasing the static gap between the beam and gate increases the amplitude of the response with a negligible change in the peak frequency. However, closer analysis shows that the changes in the length, modulus of elasticity, specific damping coefficient and gap size also influence the bandwidth of the resonant peak.

Further verification of the model was obtained by analyzing the tuning behavior of the resonant response for varying dc bias amplitudes. Figure 11 shows the impact of the gate bias, V_{dc} on both the peak amplitude and resonant frequency for the simulation and experimental data when considering a beam with $L = 6.3\text{ }\mu\text{m}$, $w = 120\text{ nm}$. For this analysis, the experimental data that was initially presented in [14]. The responses have been normalized around their values at a 2V bias in order to facilitate a qualitative comparison in the face of unrefined parameter estimates for the simulation. A quadratic increase in amplitude and decrease in frequency is present in both the simulation and experimentation. The responses are similar, even when only rough estimates of the parameters are used. While the simulation and experimental data could be used to complete a parametric study and improve the accuracy of the parameter estimates, the qualitative match between the simulation and experiment was sufficient to suggest that the model was adequately capturing the major dynamics of the system.

It should be noted that a complete parameter identification for the system would prove to be exceedingly difficult using down-mixed methods. This difficulty arises from the various

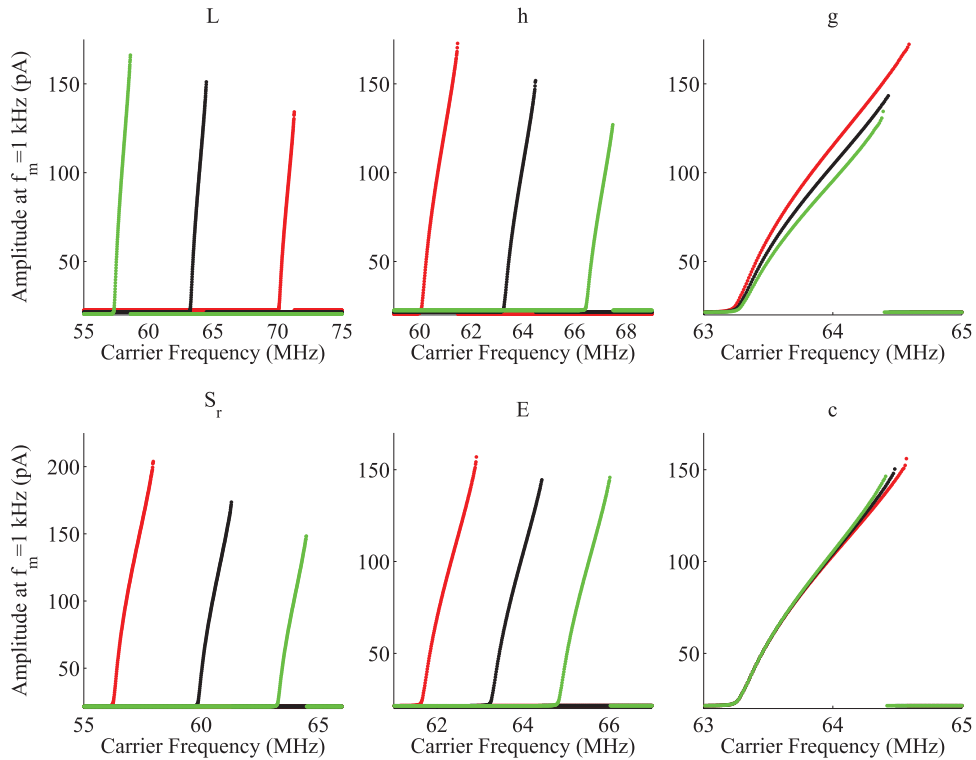


Figure 10. Simulated increasing frequency sweeps for variations in parameters. Results for each parameter are presented for their selected nominal value (black), and a 5% variation above (green) and below (red) nominal. The exception for this is the presented values of S_r , whose nominal value is 0 Pa. In this case the presented results are for -100 MPa (red), -50 MPa (black) and 0 Pa (green). All test parameters except the one under variation were held at their nominal value.

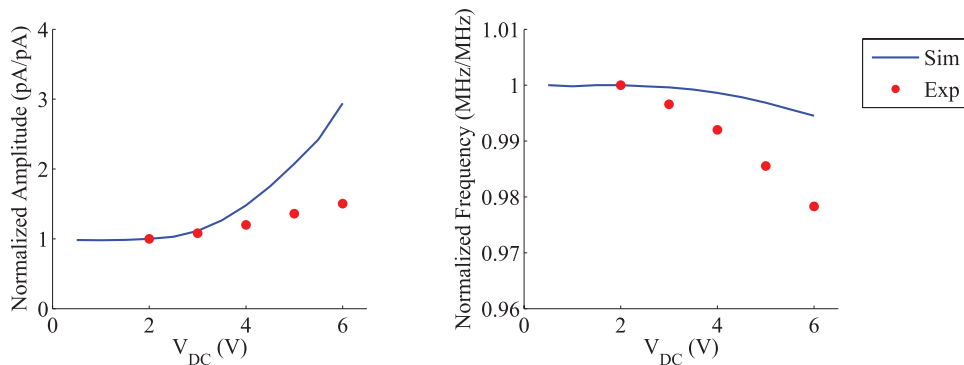


Figure 11. The effects of increasing the dc back-gate bias for a constant amplitude modulated signal across the beam, while $V_{ac} = 15$ mV_{rms}. The peak amplitude (left) and resonance frequency (right) responses are normalized around their 2V levels to facilitate qualitative comparisons in response nature. $L = 6.3$ μ m, $w = 120$ nm.

frequency regimes where the parameters affect the system. In general, several parameters have exceedingly minor effects at the low frequencies observed in the mixing methodology. This prohibits the proper identification of certain parameters when a down-mixing scheme is used, since wide variations in the parameters can have only small effects on the observed response. Reliance on the simulation instead of a closed-form analytical solution also makes parameter identification exceedingly slow. However, analytical models and an optimized testing configuration are under investigation to make system identification feasible for future studies, and the qualitative fit was considered satisfactory to provide observations on the nature of the system response with a moderate degree of accuracy.

The simulation was also used to gain a better understanding of the device from a final application perspective. While an amplitude-modulated input is representative of an input with multiple frequency components, the proposed applications for many NEMS devices do not require, or even desire, mixing (with a few exceptions, i.e. [36]). Therefore, the simulation was used to predict the system's response to a single-frequency input, measuring the amplitude and phase of the current at the same frequency output. This was done with the same test circuit used in the modulation testing, just with different input/output signal configurations. Note that no power correction is made between the signals to account for the loss of the side bands from the modulated signal.

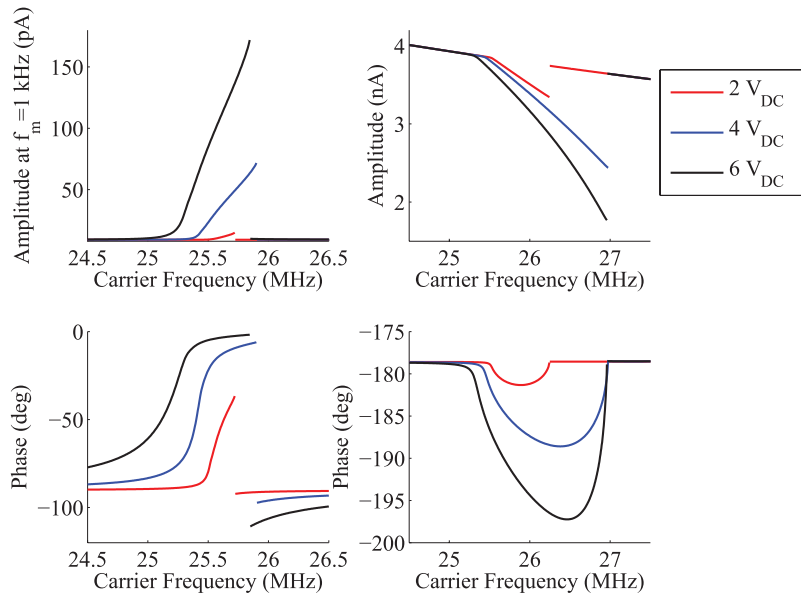


Figure 12. The amplitude (top) and phase (bottom) responses for an amplitude-modulated signal measured at the down-mixed modulation frequency (left), as well as for a single-frequency excitation, measured at that frequency (right), as the dc amplitude of the gate bias is increased. Note the change in the shape of the responses, as well as in the resonant frequencies and tuning behavior as V_{DC} changes. Also note, $V_{ac} = 40 \text{ mV}_{rms}$, $L = 6.3 \mu\text{m}$, and $w = 120 \text{ nm}$.

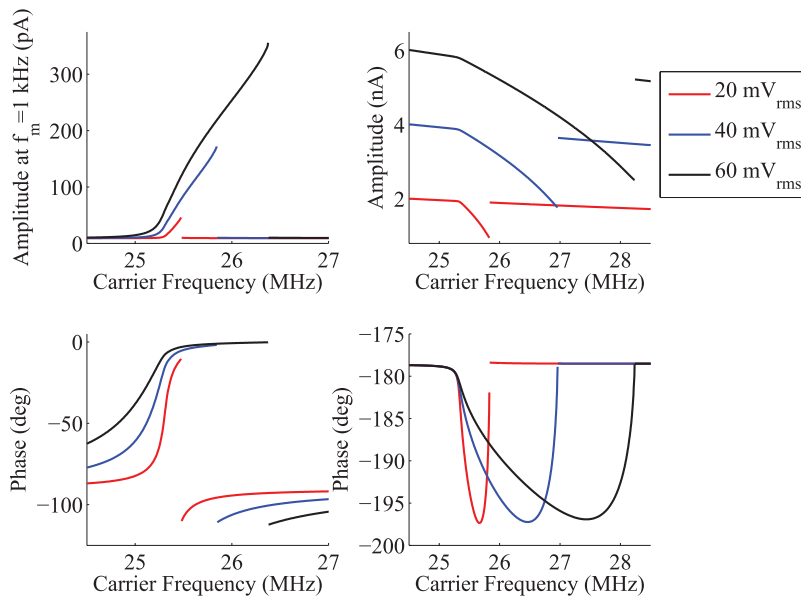


Figure 13. The amplitude (top) and phase (bottom) responses for an amplitude-modulated signal measured at the down-mixed modulation frequency (left), as well as for a single-frequency excitation, measured at that frequency (right), as the ac amplitude of the signal is increased. Note the change in the shape of the responses, as well as in the resonant frequencies as V_{ac} changes. Also note, $V_{DC} = 6 \text{ V}$, $L = 6.3 \mu\text{m}$, and $w = 120 \text{ nm}$.

Figure 12 presents the responses from the simulation for sweeps of increasing frequency for both the modulated input, measured at the down-mixed frequency, as well as a single frequency input, measured at the excitation frequency. A qualitative change in both the amplitude and phase response is immediately apparent, especially as the resonant peak becomes an antiresonance. Equally importantly is that the location of the resonant peak changes between the cases. For the modulation case, the resonant frequency is around 25.75 MHz. However, when only the single input frequency is used, the resonant frequency is varying around 26.75 MHz. The

difference in behavior exposes an issue with the methodologies common in testing NEMS to date. If the modulation case does not accurately predict the resonant frequency or tuning behavior for cases similar to possible final applications, such as a single-frequency excitation, then the devices cannot be properly designed for those final-use cases. Figure 13 shows a similar issue, for variations in the ac voltage of the carrier, while maintaining a constant dc bias. Even if a single-frequency input does not fully represent a final-use case, the presence of a resonant shift for an input variation implies that accurate predictions cannot be made using down-mixed

testing. Reference [8] exhibits a similar shift in system resonance frequency as they change from frequency-modulated testing to amplitude-modulated testing. As an aside, it is interesting to note that the tuning behavior in figure 12 does not match the curve in figure 11. This implies that the tuning curve varies with the ac amplitude applied, which is a reasonable conclusion considering the nonlinear nature of the system. Both the ac and dc variations show differences in the amount of tuning observed when comparing a modulated case to a single-frequency case. Further considering the difficulties that a mixing methodology presents with regards to proper parameter identification only serves to further complicate any device implementation based upon down-mixed data.

The development of NEMS for final usage at any level depends on understanding how the associated device will respond to stimuli when in use. Because the classical mixing methods used for testing fail to capture all of the response behavior in the regime where devices, such as the nanoresonator presented here, will be operating, the responses and properties from the modulated data, especially the system resonant frequency, cannot be used to predict the device's behavior in a final application. For example, if the system were to be used in a tunable filter design and built to operate at a frequency and dc bias determined from the down-mixed data, then the results presented here suggest that there is no guarantee the final passband of the filter would be where it was designed to be. In fact, the variation between the modulation and single-frequency cases suggests that the filter would experience changes in its passband location as the number of frequency components it receives varies, essentially negating its usefulness as a filter. This is made evident by the shifts in the system resonance frequency as the amplitude of the applied ac current is increased. Any practical application of a filter is likely to receive a signal with a changing number of frequency components and amplitudes, and both changes have been shown to produce variations in the system resonance frequency. Either a test procedure must be developed to enable accurate testing of NEMS devices in final-use scenarios, or testing is needed to determine if there is a region, perhaps under a larger dc bias, where the changes in the ac signal have less of an impact upon the nature of the device response. If such a region were to exist, then the down-mixed results may be a more appropriate predictor of device behavior.

5. Conclusions

The modeling of a nanoelectromechanical system with resonant behavior was discussed, with a focus on the development of the electrical outputs of the system arising from both capacitance modulation and piezoresistive effects present in the nanoresonator. These mechanisms were described in an equivalent circuit with approximations for the rest of the experimental setup to allow for accurate comparisons between theory and experimentation. The test circuit and device were then simulated using Verilog-A in conjunction

with Spectre's harmonic balance solver in order to verify the accuracy of the model through comparisons to experimental results. The model and simulation were qualitatively validated by comparing its response to experimental data for both amplitude and phase responses, as well as for the tuning behavior of the system under varying dc biases. Comparisons were made between the simulation results for mixing and single-frequency excitation cases, exposing discrepancies between the resonant behavior predicted experimentally and how the device may actually behave in a final-use scenario. This is an issue that must be addressed in order to develop M/NEMS components that can be designed for final applications and mass production cases alongside existing electrical systems.

Acknowledgments

The authors would like to thank Hossein Pajouhi for his technical input. This work was funded under National Science Foundation (NSF) grants 1233780 and 1247893.

Appendix A

Table A1. EOM coefficients.

Coefficient	Expression
B_0	$\rho A \int_0^L \phi^2 dx$
B_1	$c \int_0^L \phi^2 dx$
B_2	$EI_b \int_0^L \phi''' \phi dx - S_r w h \int_0^L \phi'' \phi dx$
B_3	$\frac{EA}{2L} \int_0^L \phi'^2 dx \int_0^L \phi'' \phi dx$
f_0	$45g^3 \int_0^L \phi dx$
f_1	$g^2 \left[90 \int_0^L \phi^2 dx - 2g^2 \left(15 \int_0^L \phi'' \phi dx + g^2 \int_0^L \phi''' \phi dx \right) \right]$
f_2	$135g \int_0^L \phi^3 dx + g^3 \left(-15 \int_0^L \phi'^2 \phi dx + 3g^2 \int_0^L \phi''^2 \phi dx + 4g^2 \int_0^L \phi''' \phi' \phi dx \right) + 2g^3 \left(-15 \int_0^L \phi'' \phi^2 dx + g^2 \int_0^L \phi''' \phi^2 dx \right)$
f_3	$180 \int_0^L \phi^4 dx - 30g^2 \int_0^L \phi'^2 \phi^2 dx - 30g^2 \int_0^L \phi'' \phi^3 dx + 48g^4 \int_0^L \phi'' \phi' \phi^2 dx$
f_c	$\frac{\epsilon_0 w V^2(t)}{90g^5}$

Table A2. Capacitance coefficients.

Coefficient	Expression
κ_1	$\frac{1}{g} \int_0^L \phi \, dx$
κ_2	$\frac{1}{g^2} \int_0^L \phi^2 \, dx + \frac{1}{3} \int_0^L \phi'^2 \, dx + \frac{g^2}{45} \left(\int_0^L \phi''^2 \, dx + 2 \int_0^L \phi'' \phi' \, dx \right)$
κ_3	$\frac{1}{45g^3} \left(45 \int_0^L \phi^3 \, dx + 6g^4 \int_0^L \phi'' \phi'^2 \, dx + 15g^2 \int_0^L \phi'^2 \phi \, dx - g^4 \int_0^L \phi''^2 \phi \, dx - 2g^4 \int_0^L \phi'' \phi' \phi \, dx \right)$

Table A3. Nominal parameter values.

Parameter	Value
E	187.5 GPa
ρ	2330 kg m ⁻³
ρ_r	225.4 μΩ·m
H	110 nm
g	144 nm
c	0.6E -6 kg (m·s) ⁻¹
S_r	0 Pa
R_{lock}	1 kΩ
R_{wr}	4 Ω
R_c	2 Ω
R_{subs}	10 TΩ
R_g	263 kΩ
R_r	1 GΩ
C_{wr}	0.6 nF
C_{pads}	1.45 fF
C_s	0.029 fF
π_L	1.403 1/GPa

References

[1] Huttel A K, Steele G A, Witkamp B, Poot M, Kouwenhoven L P and van der Zant H S J 2009 Carbon nanotubes as ultrahigh quality factor mechanical resonators *Nano Lett.* **9** 2547–52

[2] Chen K, Liu X, Kovacs A, Chappell W J and Peroulis D 2010 Antibiased electrostatic RF MEMS varactors and tunable filters *IEEE Trans. Microw. Theory Tech.* **58** 3971–81

[3] Bachtold A, Hadley P, Nakanishi T and Dekker C 2001 Logic circuits with carbon nanotube transistors *Science* **294** 1317–20

[4] Feng X L, White C J, Hajimiri A and Roukes M L 2008 A self-sustaining ultrahigh-frequency nanoelectromechanical oscillator *Nat. Nanotechnol.* **3** 342–6

[5] Chaste J, Lechner L, Morfin P, Feve G, Kontos T, Berroir J-M, Glatli D C, Happy H, Hakonen P and Placais B 2008 Single carbon nanotube transistor at GHz frequency *Nano Lett.* **8** 525–8

[6] Grogg D and Ionescu A M 2011 The vibrating body transistor *IEEE Trans. Electron Devices* **58** 2113–21

[7] Koskenuori M and Tittonen I 2008 Towards micromechanical radio: overtone excitations of a microresonator through the nonlinearities of the second and third order *J. Microelectromech. Syst.* **17** 363–9

[8] Gouttenoire V, Barois T, Perisanu S, Leclercq J-L, Purcell S T, Vincent P and Ayari A 2010 Digital and FM demodulation of a doubly clamped single-walled carbon-nanotube oscillator: towards a nanotube cell phone *Small* **6** 1060–5

[9] Lassagne B, Garcia-Sanchez D, Aguiasca A and Bachtold A 2008 Ultrasensitive mass sensing with a nanotube electromechanical resonator *Nano Lett.* **8** 3735–8

[10] Arcamone J, Sansa M, Verd J, Uranga A, Abadal G, Barniol N, van den Boogaart M, Brugger J and Perez-Murano F 2009 Nanomechanical mass sensor for spatially resolved ultrasensitive monitoring of deposition rates in stencil lithography *Small* **5** 176–80

[11] Forsen E et al 2005 Ultrasensitive mass sensor fully integrated with complementary metal-oxide-semiconductor circuitry *Appl. Phys. Lett.* **87** 043507

[12] Chaste J, Eichler A, Moser J, Ceballos G, Rurali R and Bachtold A 2012 A mechanical mass sensor with yoctogram resolution *Nat. Nanotechnol.* **7** 301–4

[13] Lopez J L, Verd J, Teva J, Murillo G, Giner J, Torres F, Uranga A, Abadal G and Barniol N 2009 Integration of RF-MEMS resonators on submicrometric commercial CMOS technologies *J. Micromech. Microeng.* **19** 015002

[14] Yu L, Pajouhi H, Nelis M R, Rhoads J F and Mohammadi S 2012 Tunable, dual-gate, silicon-on-insulator (SOI) nanoelectromechanical resonators *IEEE Trans. Nanotechnol.* **11** 1093–9

[15] Teva J, Abadal G, Uranga A, Verd J, Torres F, Lopez J L, Esteve J, Perez-Murano F and Barniol N 2008 From VHF to UHF CMOS-MEMS monolithically integrated resonators *Proc. of the IEEE 21st Int. Conf. on Micro Electro Mechanical Systems* pp 82–5

[16] Ollier E et al 2012 Ultra-scaled high-frequency single-crystal Si NEMS resonators and their front-end co-integration with CMOS for high sensitivity applications *Proc. of the IEEE 25th Int. Conf. on Micro Electro Mechanical Systems* pp 1368–71

[17] Huang X M H, Zorman C A, Mehregany M and Roukes M L 2003 Nanodevice motion at microwave frequencies *Nature* **421** 496–7

[18] Krylov S and Serentensky S 2006 Higher order correction of electrostatic pressure and its influence on the pull-in behavior of microstructures *J. Micromech. Microeng.* **16** 1382–96

[19] Bhushan B and Agrawal G B 2002 Stress analysis of nanostructures using a finite element method *Nanotechnology* **13** 515–23

[20] Hamad E and Omar A 2006 An improved two-dimensional coupled electrostatic-mechanical model for RF MEMS switches *J. Micromech. Microeng.* **16** 1424–9

[21] O'Mahony C, Hill M, Duane R and Mathewson A 2003 Analysis of electromechanical boundary effects on the pull-in of micromachined fixed-fixed beams *J. Micromech. Microeng.* **13** S75–80

[22] Tay F, Jun X, Liang Y, Logeeswaran V J and Yufeng Y 1999 The effects of non-parallel plates in a differential capacitive microaccelerometer *J. Micromech. Microeng.* **9** 283–93

[23] Cleland A N 2005 Thermomechanical noise limits on parametric sensing with nanomechanical resonators *New J. Phys.* **7** 1–16

[24] Judge J A, Photiadis D M, Vignola J F, Houston B H and Jarzynski J 2007 Attachment loss of micromechanical and nanomechanical resonators in the limits of thick and thin support structures *J. Appl. Phys.* **101** 013521

- [25] Judge J A, Vignola J F and Jarzynski J 2008 Dissipation from microscale and nanoscale beam resonators into a surrounding fluid *Appl. Phys. Lett.* **92** 124102
- [26] Ai S and Pelesko J A 2008 Dynamics of a canonical electrostatic MEMS/NEMS system *J. Dyn. Differ. Equ.* **20** 609–41
- [27] Conley W G, Raman A, Krousgrill C M and Mohammadi S 2008 Nonlinear and non-planar dynamics of suspended nanotube and nanowire resonators *Nano Lett.* **8** 1590–5
- [28] Vyas A, Bajaj A K, Raman A and Peroulis D 2006 Nonlinear micromechanical filters based on internal resonance phenomenon *IEEE Proc. of the Topical Meeting on Silicon Monolithic Integrated Circuits in RF Systems* pp 35–8
- [29] Batra R C, Porfiri M and Spinello D 2007 Review of modeling electrostatically actuated microelectromechanical systems *Smart Mater. Struct.* **16** R23–R31
- [30] Lifshitz R and Roukes M L 2000 Thermoelastic damping in micro- and nanomechanical systems *Phys. Rev. B* **61** 5600–9
- [31] Abdel-Rahman E M, Younis M I and Nayfeh A H 2002 Characterization of the mechanical behavior of an electrically actuated microbeam *J. Micromech. Microeng.* **12** 759–66
- [32] Ouakad H M and Younis M I 2009 Nonlinear dynamics of electrically actuated carbon nanotube resonators *J. Comput. Nonlinear Dyn.* **5** 011009
- [33] Eichler A, Moser J, Chaste J, Zdrojek M, Wilson-Rae I and Bachtold A 2011 Nonlinear damping in mechanical resonators made from carbon nanotubes and graphene *Nat. Nanotechnol.* **6** 339–42
- [34] Uranga A, Verd J, Marigo E, Giner J, Munoz-Gamarrá J L and Barniol N 2013 Exploitation of non-linearities in CMOS-NEMS electrostatic resonators for mechanical memories *Sensors Actuators A* **197** 88–95
- [35] Garcia-Sanchez D, San Paulo A, Esplandiú M J, Perez-Murano F, Forró L, Aguasca A and Bachtold A 2007 Mechanical detection of carbon nanotube resonator vibrations *Phys. Rev. Lett.* **99** 085501
- [36] Uranga A, Verd J, Lopez J L, Teva J, Abadal G, Torres F, Esteve J, Perez-Murano F and Barniol N 2007 Fully integrated mixer based on VHF CMOS-MEMS clamped-clamped beam resonator *Electron. Lett.* **43** 452–4
- [37] Candler R N, Li H, Lutz M, Park W-T, Partridge A, Yama G and Kenny T W 2003 Investigation of energy loss mechanisms in micromechanical resonators *IEEE Proc. of the 12th Int. Conf. on Solid-State Sensors, Actuators and Microsystems* vol 1 pp 332–5
- [38] Yasumura K Y, Stowe T D, Chow E M, Pfafman T, Kenny T W, Stipe B C and Rugar D 2000 Quality factors in micron- and submicron-thick cantilevers *J. Microelectromech. Syst.* **9** 117–25
- [39] Sazonova V, Yaish Y, Ustunel H, Roundy D, Arias T A and McEuen P L 2004 A tunable carbon nanotube electromechanical oscillator *Nature* **431** 284–7
- [40] Sabater A, Kumar V, Mahmood A and Rhoads J F 2013 On the nonlinear dynamics of electromagnetically transduced microresonators *J. Microelectromech. Syst.* **22** 1020–31
- [41] He R, Feng X L, Roukes M L and Yang P 2008 Self-transducing silicon nanowire electromechanical systems at room temperature *Nano Lett.* **8** 1756–61
- [42] Truitt P A, Hertzberg J B, Altunkaya E and Schwab K C 2013 Linear and nonlinear coupling between transverse modes of a nanomechanical resonator *J. Appl. Phys.* **114** 114307
- [43] Lin A T H, Lee J E Y, Yan J and Seshia A A 2010 Methods for enhanced electrical transduction and characterization of micromechanical resonators *Sensors Actuators A* **158** 263–72
- [44] Koskenuvuori M and Tittonen I 2007 Improvement of the conversion performance of a resonating multimode microelectromechanical mixer-filter through parametric amplification *IEEE Electron Device Lett.* **28** 970–2
- [45] Witkamp B, Poot M and van der Zant H S J 2006 Bending-mode vibration of a suspended nanotube resonator *Nano Lett.* **6** 2904–8
- [46] He R and Yang P 2006 Giant piezoresistance effect in silicon nanowires *Nat. Nanotechnol.* **1** 42–6
- [47] Postma H W C, Kozinsky I, Husain A and Roukes M L 2005 Dynamic range of nanotube- and nanowire-based electromechanical systems *Appl. Phys. Lett.* **86** 223105
- [48] Kozinsky I, Postma H W C, Bargatin I and Roukes M L 2006 Tuning nonlinearity, dynamic range, and frequency of nanomechanical resonators *Appl. Phys. Lett.* **88** 253101
- [49] Koskenuvuori M and Tittonen I 2008 GHz-range FSK-reception with microelectromechanical resonators *Sensors Actuators A* **142** 346–51
- [50] Yang F, Chong A C M, Lam D C C and Tong P 2002 Couple stress based strain gradient theory for elasticity *Int. J. Solids Struct.* **39** 2731–43
- [51] Stolken J S and Evans A G 1998 A microbend test method for measuring the plasticity length scale *Acta Mater.* **46** 5109–15
- [52] Chong A C M, Yang F, Lam D C C and Tong P 2001 Torsion and bending of micron-scaled structures *J. Mater. Res.* **16** 1052–8
- [53] Ouakad H M and Younis M I 2011 Natural frequencies and mode shapes of initially curved carbon nanotube resonators under electric excitation *J. Sound Vib.* **330** 3182–95
- [54] Blom F R, Bouwstra S, Elwenspoek M and Fluitman J H J 1992 Dependence of the quality factor of micromachined silicon beam resonators on pressure and geometry *J. Vacuum Sci. Technol. B* **10** 19–26
- [55] Braginsky V B, Mitrofanov V P and Panov V I 1985 *Systems With Small Dissipation* (Chicago, IL: University of Chicago Press)
- [56] Batra R C, Porfiri M and Spinello D 2006 Capacitance estimate for electrostatically actuated narrow microbeams *Micro Nano Lett.* **1** 71–3
- [57] Kanda Y 1982 A graphical representation of the piezoresistance coefficients in silicon *IEEE Trans. Electron Devices* **29** 64–70
- [58] Younis M I 2011 *MEMS Linear and Nonlinear Statics and Dynamics* vol 20 (Berlin: Springer)
- [59] Wortman J J and Evans R A 1965 Young's modulus, shear modulus, and Poisson's ratio in silicon and germanium *J. Appl. Phys.* **36** 153–6